ACS APPLIED MATERIALS & INTERFACES

www.acsami.org

Research Article

Boosting Low-Temperature Resistance of Energy Storage Devices by Photothermal Conversion Effects

Fei Yu, Jialun Li, Yi Jiang, Liying Wang, Xijia Yang, Xuesong Li, Wei Lü,* and Xiaojuan Sun*

Cite This: *ACS Appl. Mater. Interfaces* 2022, 14, 23400−23407

Read Online

ACCESS | Metrics & More | Article Recommendations | Supporting Information

ABSTRACT: While flexible supercapacitors with high capacitance and energy density is highly desired for outdoor wearable electronics, their application under low-temperature environments, like other energy storage devices, remains an urgent challenge. Solar thermal energy converts solar light into heat and has been extensively applied for solar desalination and power generation. In the present work, to address the failure problem of energy storage devices in a cold environment, solar thermal energy was used to improve flexible supercapacitor performance at low temperature. As a proof of concept presented here, a typical all-solid-state supercapacitor composed of activated carbon electrodes and gel polymer electrolyte was coated by a carbonized melamine sponge. Due to the ability of photothermal conversion of carbonized melamine sponge, the capacitance of the supercapacitor was greatly enhanced, which could be further improved by adding surface plasmonic nanomaterials, for example, Ag nanowires. Compared with the device without photothermal conversion layers, the specific capacitance increased 3.48 times at −20 °C and retained 87% capacitance at room temperature and the specific capacitance increased 6.69 times at −50 °C and retained 73% capacitance at room temperature. The present work may provide new insights on the application of solar energy and the design of energy storage devices with excellent low-temperature resistance.

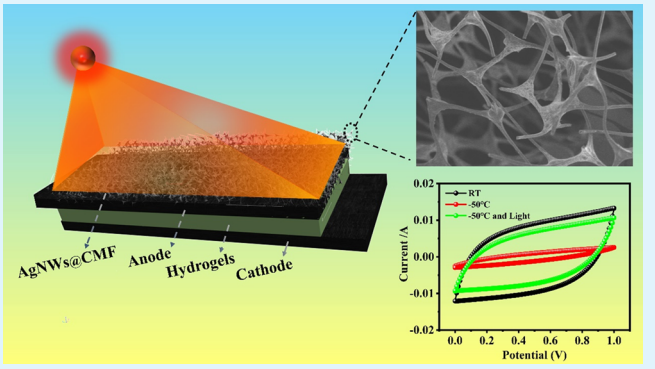

KEYWORDS: *photothermal conversion, supercapacitor, low-temperature resistance, carbonized sponge, energy storage*

1. INTRODUCTION

In the recent two decades, with the rapid development of smart and portable electronic devices, as power supply parts, the corresponding energy storage devices such as Li-ion batteries and supercapacitors (SCs) with high energy density and power density have become highly desired and have been intensively investigated.[1−3] SCs as one of the most important energy storage devices mainly include double-layer capacitors based on ion cladding/decoupling and pseudocapacitors based on the Faraday reaction, which have numerous potential applications in hybrid vehicles, personal portable electronic devices, aerospace power supplies, and so on.[3−5] While flexible SCs with high capacitance and energy density are highly desired for outdoor wearable electronics, their application under low-temperature environments, like other energy storage devices, remains an urgent challenge.[3,6−8] In spite of the inspiring progress in low-temperature-resistant electrolyte, the deactivation of electrolyte cannot be fully avoided with the decreasing temperatures and thus SC performance in cold environments is still unsatisfactory.[9]

Solar energy is one of green and renewable energies. The utilization of solar energy mainly includes photocatalysis, photovoltaic power generation, and photothermal conversion.[10] The photothermal effect refers to a phenomenon in which photon energy interacts with the lattice when a material is irradiated by light, intensifying the vibration and increasing the temperature, and can be observed in inorganic materials such as precious metals and semiconductors, as well as organic materials such as carbon-based materials, dyes, and conjugated polymers.[10−14] An ideal photothermal material should have high photothermal efficiency, light absorption rate, and low reflectivity.[15,16]

To improve low-temperature resistance of energy storage devices, the integration of photothermal materials with energy storage devices could be an effective strategy. Photothermal materials can be introduced as photothermal coating films or electrode materials when constructing devices for low temperature, thus maintaining the actual operating temperature of SCs and alleviating the capacity deterioration in a low-

Received: February 19, 2022
Accepted: April 27, 2022
Published: May 10, 2022

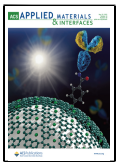

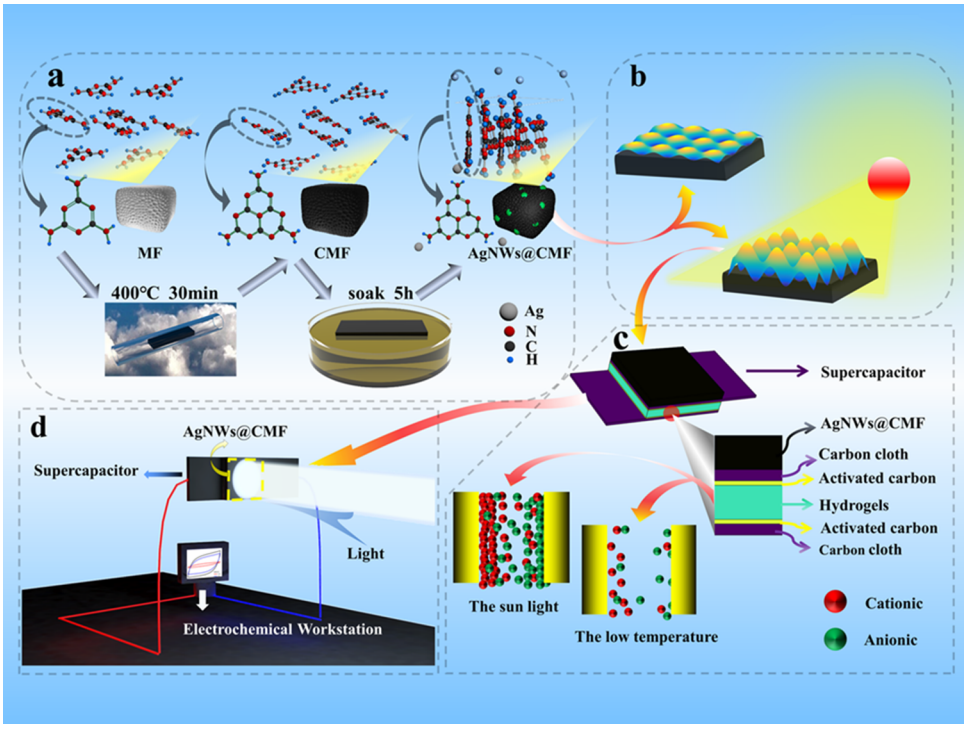

Figure 1. Schematic illustration of (a) preparation process of AgNWs@CMF, (b) surface plasmon resonance of AgNWs@CMF under illumination, (c) SC covered by AgNWs@CMF, and (d) test configuration of the photothermal SC working under illumination.

temperature environment. The actual operating temperature of devices in a low-temperature environment has been reported to be improved by photothermal self-heating films.[11,17−19] The electrodes that serve as both electroactive components and photothermal layers are also developed for constructing high-performance antifreezing energy storage units.[13,20,21] While these works did improve low-temperature operation performance of energy storage devices, complicated procedures and high cost were generally involved, thus limiting the extensive commercial application. Therefore, it is necessary to develop a facile, economic, and efficient way to integrate the photothermal effect into energy storage devices.

In this work, we reported a strategy to improve energy storage device performance by integrating photothermal conversion films onto flexible SCs. The carbonized melamine sponge (CMF) derived from commercially available melamine sponge (MF) was used as photothermal materials, and the flexible SCs were composed of activated carbon electrodes and gel polymer electrolyte. Due to the ability of photothermal conversion of CMF, the capacitance of SCs was greatly enhanced, which could be further improved by adding Ag nanowires (AgNWs@CMF). Compared with the device without photothermal conversion layers, the specific capacitance increased 3.48 times and 6.69 times at −20 and −50 °C, respectively. The present work provided a feasible and facile way to improve low-temperature resistance of energy storage devices, which could be easily expanded to practical industrialized application.

2. EXPERIMENTAL SECTION

2.1. Preparation of AgNWs. Typically, a 60 mL solution of PVP (0.18 mol/L) in ethylene glycol (EG) was prepared. After addition of 30 μL of NaCl (0.1 mol/L), the solution was heated to 170 °C for 1.5 h under stirring. Then, 30 mL of $AgNO_3$ solution (0.12 mol/L) in EG was added and kept at 170 °C for another 2.5 h. The resulted product was centrifuged and washed to acquire AgNWs.[22]

2.2. Preparation of CMF and AgNWs@CMF. The commercial MF foam was cut into suitable size, which was subsequently washed and dried at 80 °C. Then, the MF was sintered at 400 °C for 2 h in nitrogen. The CMF was acquired after cooling to room temperature (RT). Then, it was dipped in AgNW solution for 10 min to acquire AgNWs@CMF.[23,24]

2.3. Preparation of Electrolyte and Assembling of SCs. Typically, suitable PVA was dissolved in a glycerol/water solution with a volume ratio of 2:3 under stirring at 100 °C. Then, 3 M LiCl was added.[25,26]After removing the bubbles, the solution was poured into a glass mold and placed in vacuum to obtain a transparent gel. Activated carbon, conductive carbon black, and tetrafluoroethylene are mixed at a ratio of 8:1:1, which was further coated on carbon cloths as electrodes. The gel electrolyte was sandwiched between two pieces of electrodes to finish a SC device.[27,28]

2.4. Characterization. The surface morphologies and structures of materials were analyzed by scanning electron microscopy (SEM, Zeiss Merlin Compact), X-ray diffraction (XRD, D/max 2550 V X-ray diffractometer, Rigaku Japan), and Raman spectroscopy (Horiba Jobin Yvon, LabRAM HR Evolution). The electrochemical test and the photoelectrochemical test were carried out using a CHI660E electrochemical workstation.

3. RESULTS AND DISCUSSION

The 3D structure of AgNWs@CMF was fabricated by a two-step process as shown in Figure 1a. At first, the MF was calcined at 400 °C for 30 min in nitrogen to acquire CMF. The thermogravimetric analysis (TGA) (Figure S1a in the Supporting Information) reveals that the weight loss before 400 °C is due to the evaporation of water, the volatilization of NH_3 and the formation of melamine, and the transformation of melamine to melem, respectively.[29] Calcination induces volume shrinkage and color change of MF from white to black as shown in Figure S1b in the Supporting Information. Second, the obtained CMF was immersed in a solution

https://doi.org/10.1021/acsami.2c03124
ACS Appl. Mater. Interfaces 2022, 14, 23400−23407

including AgNWs and dried to acquire AgNWs@CMF. Figure 1b shows a schematic diagram of enhanced light absorption due to the surface plasmon resonance of AgNWs in the CMF matrix. Due to the porous structure of CMF and addition of AgNWs, AgNWs@CMF exhibits a high photothermal effect, an enhanced light absorption rate, and low reflectivity and is expected to provided photothermal energy to SCs for enhancing low-temperature resistance. Figure 1c is a proof of concept presented, and a typical all-solid-state SC composed of activated carbon electrodes and gel polymer electrolyte was coated by AgNWs@CMF. Figure S2 in the Supporting Information describes the detailed structure of the device. AgNWs@CMF as the photothermal layer generates heat under illumination and transfers it to the top electrode, gel electrolyte, and the bottom electrode of SCs in sequence. The distribution of the temperature field is shown in the right of Figure S2. The low-temperature resistance of the device is tested under illumination as shown in Figure 1d.

Figure 2a,b shows SEM images of MF with different magnifications, and the interconnected 3D structure could be observed. After sintering at 400 °C, the white MF became black CMF foam but still had certain elasticity. The structure of CMF is shown in Figure 2c,d. Compared with MF, the pore size of the CMF porous structure is slightly reduced and partially broken, which is due to the release of NH_3 by combining H bonds and N bonds in MF during the carbonization process.[30] For AgNWs@CMF, as shown in Figure 2e,f, the surface of CMF attracted a large amount of AgNWs, which are uniformly dispersed on the CMF skeleton. Figure 2g shows the XRD curves of CMF and AgNWs@CMF. For CMF, the broad diffraction peak between 20° and 30° is a typical feature of carbon materials. For AgNWs@CMF, the broad peak between 20° and 30° is faded by the sharp peaks of Ag at 38.1°, 44.3°,64.4°,77.5°, and 81.5°, which corresponds to (111), (200), (220), (311), and (222) diffraction of Ag. Figure 2h shows the absorption spectra of MF and AgNWs@CMF. It could be observed that high temperature carbonization of MF and the addition of AgNWs greatly enhanced the absorption, which is beneficial for photothermal conversion. The resulted black CMF is composed of the carbon skeleton. Due to the light trapping structure of the porous carbon skeleton and the enhanced absorption of sunlight provided by surface plasmon resonance of AgNWs, the overall absorption is greatly enhanced. Figure 2i shows the Raman spectra of MF and CMF. The D band around 1300 cm^{-1} reflects the defect states of the carbon lattice, and the G band around 1580 cm^{-1} represents the in-plane stretching vibration of the sp^2 hybridization of C atoms. The ratio of I_D/I_G decreased from 1.063 to 0.966 after carbonization, indicating the formation of the carbon skeleton, and the lattice vibration in CMF is more continuous, which is beneficial to reducing the propagation of phonons and enhance the photothermal conversion ability of CMF.[31,32] The peaks at 1058 and 2964 cm^{-1} in MF are caused by the stretching vibration of N−N−N rings and C−H bonds. After carbonization, the two peaks are substantially depressed due to removing H, O, and N elements.

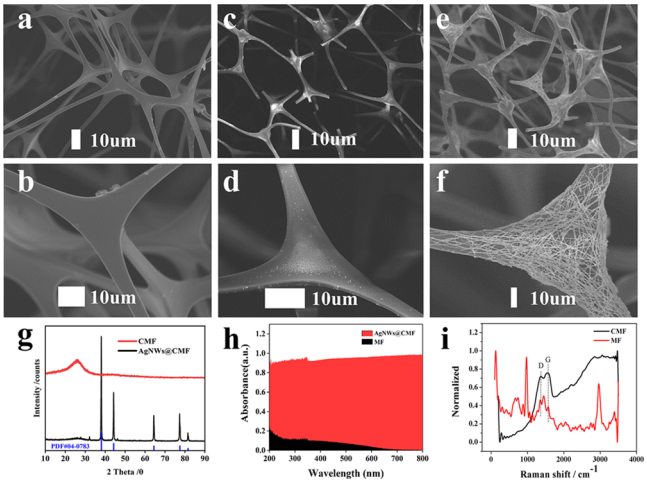

Figure 2. SEM images of MF (a and b), CMF (c and d), and AgNWs@CMF (e and f); (g) XRD curves of CMF and AgNWs@CMF; (h) absorption spectra of MF and AgNWs@CMF; and (i) Raman spectra of CMF and AgNWs@CMF.

Figure 3a shows the surface temperature variation of MF, CMF, and AgNWs@CMF under one sun illumination as a function of illumination time. While the surface temperature of MF increased from 29.8° to 31.7° in 30 s, that of CMF increased from 30.0° to 56.0°, indicating the better photothermal conversion ability of CMF. After combination with

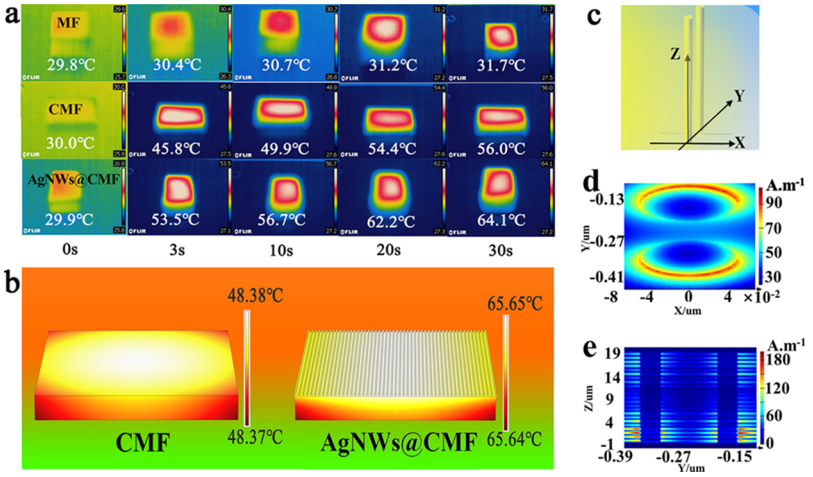

Figure 3. (a) Surface temperature variations of MF, CMF, and AgNWs@CMF as a function of illumination time; (b) simulation of the CMF temperature field with or without AgNWs; and (c−e) FTDT simulation of the surface electromagnetic field distribution on the surface of AgNWs.

https://doi.org/10.1021/acsami.2c03124
ACS Appl. Mater. Interfaces 2022, 14, 23400−23407

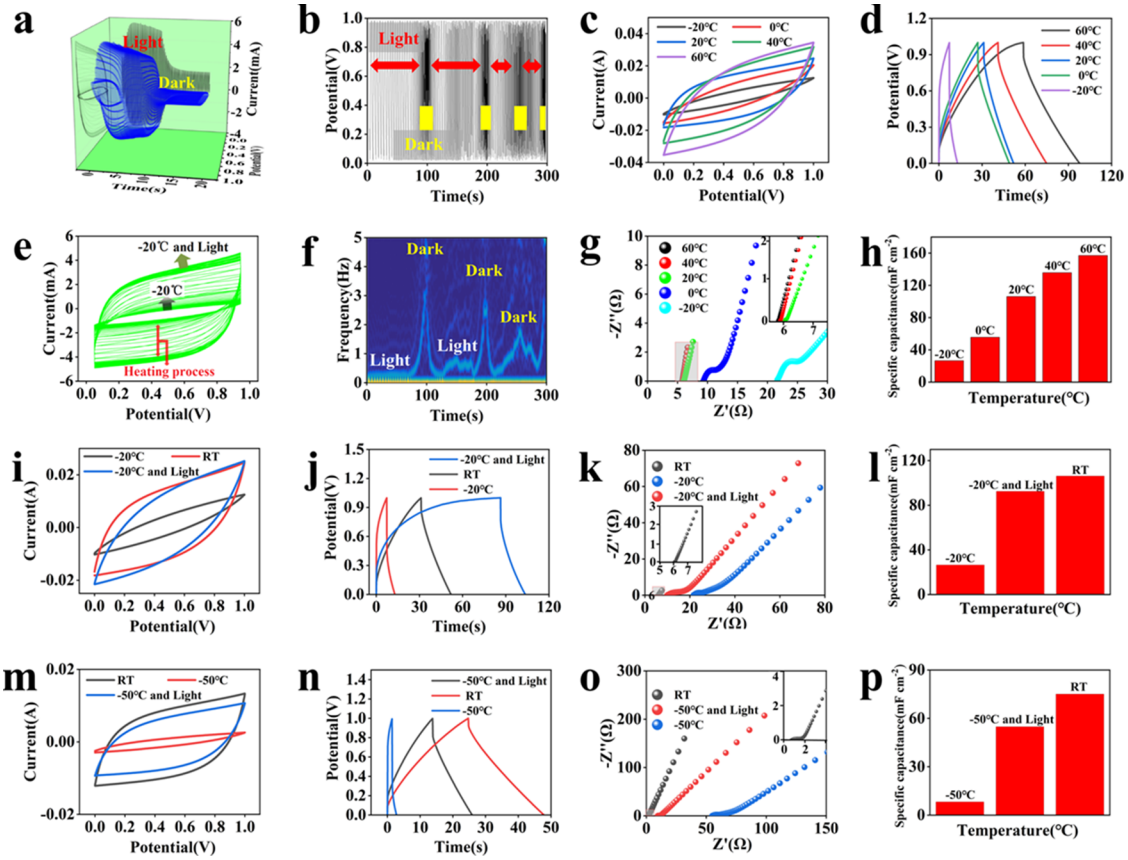

Figure 4. (a) Cyclic voltammetry (CV) curves of SCs as a function of time measured at −20 °C; (b) galvanostatic charge/discharge (GCD) curves of SCs measured at −20 °C with intermittent illumination, and the illumination is shut down during 70−80, 180−190, 230−240, and 275−300 s; (c) and (d) are CV and GCD curves measured at different temperatures in the dark; (e) CV curves measured at −20 °C, which is started under illumination and the light is withdrawn after the test; (f) frequency variation as a function of time during the CV test at −20 °C; (g) Nyquist curves measured at different temperatures in the dark; (h) specific capacitance of SCs at different temperatures; (i−l) are the electrochemical performance of SCs measured at −20 °C; and (m−p) are the electrochemical performance of SCs measured at −50 °C.

AgNWs, the surface temperature increased from 30.0° to 64.1° in 30 s, confirming that the surface plasmon resonance of AgNWs would further enhance the photothermal effect. The thermal conductivities of MF and CMF are 0.33 and 0.38 W m^{-1} K^{-1}, respectively. In the present work, the thickness of the photothermal layer is in the range of millimeters, and the heat transfer distance between the photothermal layer and the electrode surface is greatly reduced, which inhibits the heat diffusion to air and improves the overall capacity utilization efficiency.[29] The effect of the photothermal layer thickness on device performance will be discussed later as shown in Figure S6 in the Supporting Information. Figure S3 in the Supporting Information shows the surface temperature of AgNWs@CMF with and without illumination measured in a −50 °C environment. The temperature increases rapidly near RT upon illumination even in an extremely cold environment and the calculated photothermal conversion efficiency is 91.5% as shown in the Supporting Information, indicating the excellent photothermal conversion ability of AgNWs@CMF.

Figure 3b shows the simulation of the photothermal effect. The left one is a piece of the CMF material, and the right one is the same CMF coated with AgNWs. Upon illumination, the maximum surface temperature of CMF and AgNWs@CMF was 48.38 and 65.65 °C, respectively. The simulation is based on the plasmon resonance excitation of AgNWs coated on the surface of the CMF by the external incident light source and is well consistent with experimental results.[33−37] The surface plasmon resonance-induced absorption enhancement is further analyzed by theoretical simulations. Figure 3c shows two AgNWs under parallel illumination from the *X*-direction. Figure 3d shows the top view of magnetic field distribution. It can be seen that the strongest magnetic field intensity occurs near the surface of AgNWs and which gradually decreases in the direction away from the surface. Figure 3e shows the plane view of the magnetic field distribution, which exhibits a periodic distribution behavior on the cross-sectional surface, indicating that the plasma on the surface of AgNWs will propagate in the form of bulk waves and then disappear. The surface plasmon resonance increases the probability of electron collision on the surface of AgNWs. When electrons jump from the Fermi energy level to the higher energy level, superhot electrons are generated due to thermal motion, and the energy captured by the surface plasma is released through electron−phonon scattering, which intensifies the oscillation of the surface plasma, that is, thermal energy.[23,38−40] The thermal energy is then transported to the external environment through the relaxation generated during the phonon−phonon vibration. Figure S4b−f in the Supporting Information shows the simulation with the same method at different cross-sectional depths as shown in Figure S4a, and the similar results could be confirmed.

https://doi.org/10.1021/acsami.2c03124
ACS Appl. Mater. Interfaces 2022, 14, 23400−23407

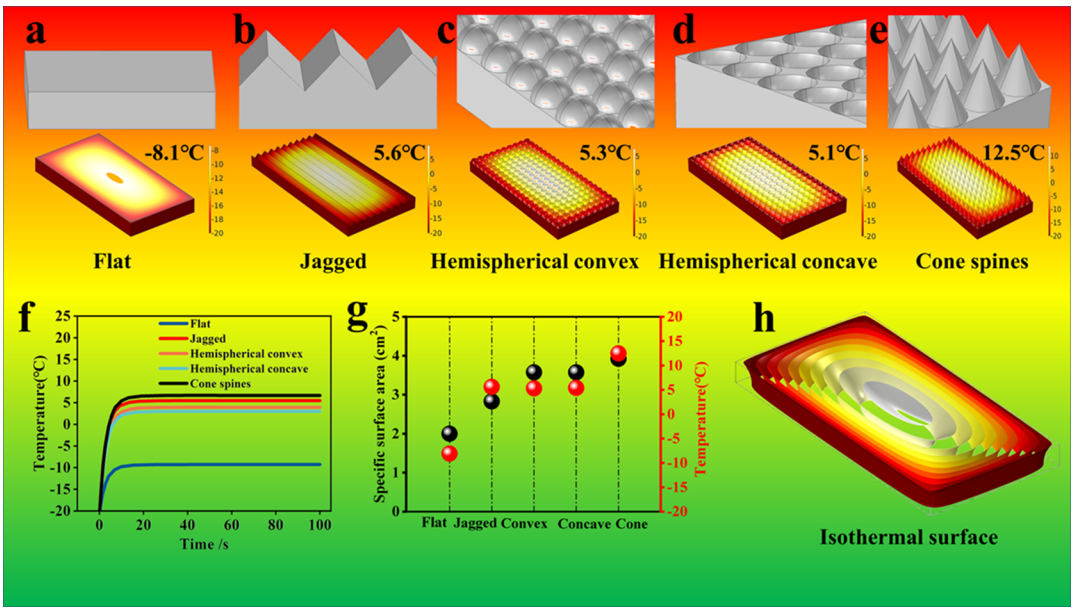

Figure 5. Theoretical simulation of the effect of surface morphology on photothermal conversion efficiency. (a−e) Different surface morphologies and corresponding temperature fields; (f) temperature variation of the five morphologies at 1.5 mm depth below the surface as a function of illumination time; (g) surface area and maximum temperature of different surface morphologies; and (h) temperature distribution of the surface for AgNWs@CMF.

Figure S5 in the Supporting Information shows the performance comparison of SCs with MF, CMF, and AgNWs@CMF as photothermal layers, respectively. Due to the best photothermal conversion ability of AgNWs@CMF, the SCs using AgNWs@CMF conversion layers show the best performance, which achieves the smallest resistance and the largest specific capacitance. After confirming this point, the effect of different thicknesses of the AgNWs@CMF film (1.0, 1.5, and 3.0 mm) on device performance is further investigated and shown in Figure S6 in the Supporting Information. Apparently, the 1.5 mm sample shows the best performance both in resistance and specific capacitance. This is because under illumination at −20 °C, in addition to photothermal conversion on the surface of AgNWs@CMF, heat convection of air would occur due to the porous structure. If the thickness of AgNWs@CMF is too thin, the light absorption rate will be reduced and the effective surface area for photothermal conversion will be reduced. If it is too thick, the heat will be difficult to reach the surface of the SC due to the lengthened distance for heat transport. Thus, the SC devices tested later are fabricated by AgNWs@CMF with a 1.5 mm thickness.

The aforementioned investigation has confirmed the excellent photothermal conversion ability of AgNWs@CMF, and it was further used as a photothermal conversion layer and integrated with the flexible SCs to improve the low-temperature resistance as illustrated in Figure 1c. Figure 4a shows the CV curves of SCs as a function of time under one sun illumination measured at −20 °C. Before testing, the as-prepared flexible SCs was kept at −20 °C for 30 s. During 0−1 s, the CV is measured without illumination, and the area of the CV curve is small, indicating the weakened energy storage ability, which is due to the decreased ion mobility and adsorption of ions in electrode materials induced by low temperature. Upon illumination, the area of the CV curve expands to the maximum immediately in 1−2 s, which suggests the restoration of the energy storage ability due to the heating provided by the photothermal conversion layer, and the fast response to illumination reflects the high efficiency of the present integration device. At 6 s, the illumination is withdrawn and the capacity declines fast. These results indicate that the present strategy is feasible and effective for improving the low-temperature resistance of energy storage devices with an extremely fast response.

Figure 4b shows the test result with intermittent illumination at −20 °C as a function of time. Without illumination during 70−80, 180−190, 230−240, and 275−300 s, the GCD curve is shortened obviously, which is due to the fast discharge at low temperature. Figure 4c,d shows the CV and GCD curves measured from −20 to 60 °C. As expected, the capacity of SCs is gradually enhanced with the increasing temperature. The charging/discharging time at −20 °C is 14 s and that at 60 °C is 98 s. Figure 4e shows the CV curves measured at −20 °C, which is started under illumination. After testing, the sunlight is withdrawn and the gradually reduced CV area could be confirmed, indicating that the cooling process do impart the energy storage ability of devices. Figure 4f shows the frequency variation as a function of time during the CV test. The obvious enhancement in frequency could be observed at the time without illumination and the peak values are located at 80, 85, 235, and 285 s, which is consistent with the results in Figure 4b, and the reason is attributed to the low-temperature-induced reduction in the charging/discharging time. Figure 4g shows the Nyquist curves measured at different temperatures. The internal resistance of SCs increases with the decreasing temperatures, which is consistent with the results of the CV and GCD. Figure 4h shows the specific capacity variation as a function of temperature measured in the dark, and the specific capacity continuously decreases with the decreasing temperature, confirming the declined device performance.

Figure 4i,j shows that the capacity of SCs can be restored greatly upon illumination at −20 °C. Figure 4k shows the Nyquist curves of SCs, and it can be seen that the resistance is decreased with the photothermal conversion effect, indicating the improved performance. The specific capacitance at −20 °C

https://doi.org/10.1021/acsami.2c03124
ACS Appl. Mater. Interfaces 2022, 14, 23400−23407

in Figure 4l is 26.56 mF cm^{-1}, which increased to 92.5 mF cm^{-1} upon illumination, achieving 87% retention of RT capacitance. Figure 4m−p shows the electrochemical performance and specific capacitance of the SC measured at −50 °C and the comparison with that at RT. The specific capacitance increases 6.69 times at −50 °C upon illumination and retained 73% of RT capacitance.

While it has been shown that the photothermal conversion layer could greatly improve performance of energy storage devices, photothermal conversion efficiency would be affected by surface morphology of conversion layer materials. Therefore, the theoretical simulation of the effect of surface morphology on photothermal conversion efficiency at −20 °C under one sun illumination is carried out and shown in Figure 5.[30,40−42] Five different surface morphologies are investigated as shown in Figure 5a−e. The results indicate that the cone spine surface with the largest specific surface area has the highest surface temperature. Figure 5f shows the temperature variation at 1.5 mm depth below the surface as a function of illumination time, indicating the different efficiencies of these surfaces for photothermal conversion. Figure 5g shows a graphical comparison of the specific surface area and maximum temperature for these surface morphologies. The cone spine surface exhibits the best performance. Figure 5h shows the temperature field distribution of AgNWs@CMF under illumination, and it can be seen that the surface temperature decreases from the center to the edge, and the isothermal surface gradually decreases with the increasing depth. Although this work provides a strategy to improve low-temperature resistance of devices, we also indicate that the performance could be further enhanced by the surface structure design of the conversion layer.

4. CONCLUSIONS

In summary, a facile, economic, and efficient strategy has been developed for integrating the photothermal effect into energy storage devices. To verify the concept, an all-solid-state SC with commercial activated carbon as electrodes has been fabricated, which is covered by CMF. We have shown the low-temperature resistance of SCs has been greatly improved due to the photothermal conversion ability of CMF, and further improvement could be achieved by adding surface plasmonic nanomaterials. It has been shown by theoretical simulations that the photothermal conversion ability is dependent on the elegant design both in material choice and structure modification. This should be a feasible and economic strategy for actual application after systematic optimization.

■ ASSOCIATED CONTENT

Supporting Information

The Supporting Information is available free of charge at https://pubs.acs.org/doi/10.1021/acsami.2c03124.

TGA curve of MF, the detailed structure of the SC covered by the AgNW@CMF photothermal conversion film, surface temperature of AgNWs@CMF measured in a −50 °C environment, FDTD simulation of the surface plasmon resonance of AgNWs, electrochemical performance of SCs coated with MF, CMF, and AgNWs@CMF measured at −20 °C, electrochemical performance of supercapacitors coated by AgNWs@CMF sponge with thicknesses of 1.0, 1.5, and 3.0 mm, calculation of photothermal conversion efficiency, and the simulation method (PDF)

■ AUTHOR INFORMATION

Corresponding Authors

Wei Lü − *Key Laboratory of Advanced Structural Materials, Ministry of Education & Advanced Institute of Materials Science, Changchun University of Technology, Changchun 130012, People's Republic of China; State Key Laboratory of Luminescence and Applications, Changchun Institute of Optics, Fine Mechanics and Physics, Chinese Academy of Sciences, Changchun 130033, People's Republic of China;* orcid.org/0000-0002-7070-8456; Email: lw771119@hotmail.com

Xiaojuan Sun − *State Key Laboratory of Luminescence and Applications, Changchun Institute of Optics, Fine Mechanics and Physics, Chinese Academy of Sciences, Changchun 130033, People's Republic of China*; Email: sunxj@ciomp.ac.cn

Authors

Fei Yu − *Key Laboratory of Advanced Structural Materials, Ministry of Education & Advanced Institute of Materials Science, Changchun University of Technology, Changchun 130012, People's Republic of China*

Jialun Li − *Key Laboratory of Advanced Structural Materials, Ministry of Education & Advanced Institute of Materials Science, Changchun University of Technology, Changchun 130012, People's Republic of China*

Yi Jiang − *School of Science, Changchun Institute of Technology, Changchun 130012, China*

Liying Wang − *Key Laboratory of Advanced Structural Materials, Ministry of Education & Advanced Institute of Materials Science, Changchun University of Technology, Changchun 130012, People's Republic of China*

Xijia Yang − *Key Laboratory of Advanced Structural Materials, Ministry of Education & Advanced Institute of Materials Science, Changchun University of Technology, Changchun 130012, People's Republic of China*

Xuesong Li − *Key Laboratory of Advanced Structural Materials, Ministry of Education & Advanced Institute of Materials Science, Changchun University of Technology, Changchun 130012, People's Republic of China*

Complete contact information is available at: https://pubs.acs.org/10.1021/acsami.2c03124

Author Contributions

The manuscript was written through contributions of all authors.

Notes

The authors declare no competing financial interest.

■ ACKNOWLEDGMENTS

This work was financially supported by the National Natural Science Foundation of China (No. 62004015 and 62004014) and the Department of Science and Technology of Jilin Province (20210101077JC).

■ REFERENCES

(1) Zhao, C. T.; Yu, C.; Zhang, M. D.; Sun, Q.; Li, S. F.; Banis, M. N.; Han, X. T.; Dong, Q.; Yang, J.; Wang, G.; Sun, X. L.; Qiu, J. S. Enhanced sodium storage capability enabled by super wide-interlayer-

spacing MoS_2 integrated on carbon fibers. *Nano Energy* **2017**, *41*, 66−74.
(2) Zhao, D. D.; Wang, Y.; Zhang, Y. F. High-Performance Li-ion Batteries and Supercapacitors Based on Prospective 1-D Nanomaterials. *Nano-Micro Lett.* **2011**, *3*, 62−71.
(3) Lee, J.; An, G. H. Surface-engineered flexible fibrous supercapacitor electrode for improved electrochemical performance. *Appl. Surf. Sci.* **2021**, *539*, No. 148290.
(4) Liu, J. H.; Khanam, Z.; Ahmed, S.; Wang, H. T.; Wang, T.; Song, S. H. A study of low-temperature solid-state supercapacitors based on Al-ion conducting polymer electrolyte and graphene electrodes. *J. Power Sources* **2021**, *488*, 13.
(5) Liu, J. H.; Khanam, Z.; Ahmed, S.; Wang, T.; Wang, H. T.; Song, S. H. Flexible Antifreeze Zn-Ion Hybrid Supercapacitor Based on Gel Electrolyte with Graphene Electrodes. *ACS Appl. Mater. Interfaces* **2021**, *13*, 16454−16468.
(6) Liu, L.; Feng, Y.; Wu, W. Recent progress in printed flexible solid-state supercapacitors for portable and wearable energy storage. *J. Power Sources* **2019**, *410-411*, 69−77.
(7) Liu, L. L.; Niu, Z. Q.; Zhang, L.; Zhou, W. Y.; Chen, X. D.; Xie, S. S. Nanostructured Graphene Composite Papers for Highly Flexible and Foldable Supercapacitors. *Adv. Mater.* **2014**, *26*, 4855−4862.
(8) Liu, L. X.; Chen, W.; Zhang, H. B.; Wang, Q. W.; Guan, F. L.; Yu, Z. Z. Flexible and Multifunctional Silk Textiles with Biomimetic Leaf-Like MXene/Silver Nanowire Nanostructures for Electromagnetic Interference Shielding, Humidity Monitoring, and Self-Derived Hydrophobicity. *Adv. Funct. Mater.* **2019**, *29*, No. 1905197.
(9) Jian, Y. K.; Handschuh-Wang, S.; Zhang, J. W.; Lu, W.; Zhou, X. C.; Chen, T. Biomimetic anti-freezing polymeric hydrogels: keeping soft-wet materials active in cold environments. *Mater. Horiz.* **2021**, *8*, 351−369.
(10) Wu, M. X.; Lin, X.; Wang, T. H.; Qiu, J. S.; Ma, T. L. Low-cost dye-sensitized solar cell based on nine kinds of carbon counter electrodes. *Energy Environ. Sci.* **2011**, *4*, 2308−2315.
(11) Sun, Y. L.; Ma, P. J.; Liu, L. Y.; Chen, J. T.; Zhang, X.; Lang, J. W.; Yan, X. B. Solar-Thermal Driven Self-Heating of Micro-Supercapacitors at Low Temperatures. *Sol. RRL* **2018**, *2*, 9.
(12) Yang, R. T.; Li, D.; Salazar, S. L.; Rao, Z. H.; Arici, M.; Wei, W. Photothermal properties and photothermal conversion performance of nano-enhanced paraffin as a phase change thermal energy storage material. *Sol. Energy Mater. Sol. Cells* **2021**, *219*, 11.
(13) Yi, F.; Ren, H. Y.; Dai, K. R.; Wang, X. F.; Han, Y. Z.; Wang, K. X.; Li, K.; Guan, B. L.; Wang, J.; Tang, M.; Shan, J. Y.; Yang, H.; Zheng, M. S.; You, Z.; Wei, D.; Liu, Z. F. Solar thermal-driven capacitance enhancement of supercapacitors. *Energy Environ. Sci.* **2018**, *11*, 2016−2024.
(14) Zou, Y.; Yang, P.; Yang, L.; Li, N.; Duan, G. G.; Liu, X. H.; Li, Y. W. Boosting solar steam generation by photothermal enhanced polydopamine/wood composites. *Polymer* **2021**, *217*, 8.
(15) Xu, C.; Pu, K. Y. Second near-infrared photothermal materials for combinational nanotheranostics. *Chem. Soc. Rev.* **2021**, *50*, 1111−1137.
(16) Yin, X. M.; Li, H. J.; Yuan, R. M.; Lu, J. H. NiCoLDH nanosheets grown on MOF-derived Co3O4 triangle nanosheet arrays for high-performance supercapacitor. *J. Mater. Sci. Technol.* **2021**, *62*, 60−69.
(17) Ma, P.; Sun, Y.; Zhang, X.; Chen, J.; Yang, B.; Zhang, Q.; Gao, X.; Yan, X. Spinel-type solar-thermal conversion coatings on supercapacitors: An effective strategy for capacitance recovery at low temperatures. *Energy Storage Mater.* **2019**, *23*, 159−167.
(18) Yang, Y.; Sun, R.; Wang, X. Ag nanowires functionalized cellulose textiles for supercapacitor and photothermal conversion. *Mater. Lett.* **2017**, *189*, 248−251.
(19) He, M.; Lin, Y.-J.; Chiu, C.-M.; Yang, W.; Zhang, B.; Yun, D.; Xie, Y.; Lin, Z.-H. A flexible photo-thermoelectric nanogenerator based on MoS_2/PU photothermal layer for infrared light harvesting. *Nano Energy* **2018**, *49*, 588−595.
(20) Chen, S.; Wang, L.; Hu, X. Photothermal supercapacitors at −40 °C based on bifunctional TiN electrodes. *Chem. Eng. J.* **2021**, *423*, No. 130162.
(21) Zhao, M.; Li, Y.; Lin, F.; Xu, Y.; Chen, L.; Jiang, W.; Jiang, T.; Yang, S.; Wang, Y. A quasi-solid-state photothermal supercapacitor via enhanced solar energy harvest. *J. Mater. Chem. A* **2020**, *8*, 1829−1836.
(22) Liu, L. L.; Chen, S. X.; Xu, A. C.; Cai, G. M. Manufacturing High Sensitive Strain Sensor of Polyurethane Nanofiber Mat/AgNWs by Simple Dip-dry Method. *Fibers Polym.* **2020**, *21*, 359−365.
(23) Cheng, Y. Q.; Sun, M. T. Unified treatments for localized surface plasmon resonance and propagating surface plasmon polariton based on resonance modes in metal nanowire. *Opt. Commun.* **2021**, *499*, No. 127277.
(24) Malakar, M.; Ray, S.; Sinha, S.; Angom, D. Phases and collective modes of bosons in a triangular lattice at finite temperature: A cluster mean field study. *Phys. Rev. B* **2020**, *102*, 11.
(25) Mo, F.; Liang, G.; Wang, D.; Tang, Z.; Li, H.; Zhi, C. Biomimetic organohydrogel electrolytes for high-environmental adaptive energy storage devices. *EcoMat* **2019**, *1*, No. e12008.
(26) Wu, S.; Alsaid, Y.; Yao, B.; Yan, Y.; Zhao, Y.; Hua, M.; Wu, D.; Zhu, X.; He, X. Rapid and scalable fabrication of ultra-stretchable, anti-freezing conductive gels by cononsolvency effect. *EcoMat* **2021**, *3*, No. e12085.
(27) Yang, G.; Huang, J.; Wan, X.; Liu, B.; Zhu, Y.; Wang, J.; Fontaine, O.; Luo, S.; Hiralal, P.; Guo, Y.; Zhou, H. An aqueous zinc-ion battery working at −50 °C enabled by low-concentration perchlorate-based chaotropic salt electrolyte. *EcoMat* **2022**, *4*, No. e12165.
(28) Zhang, Y.; Wang, W.; Wang, L.; Guo, Q.; Hu, H.; Xie, C.; Shang, J.; Xu, J.; Zhang, Y.; Zheng, Z. Inverse Opaline Metallic Membrane Addresses the Tradeoff Between Volumetric Capacitance and Areal Capacitance of Supercapacitor. *Adv. Energy Mater.* **2022**, *12*, No. 2102802.
(29) Gong, F.; Li, H.; Wang, W.; Huang, J.; Xia, D.; Liao, J.; Wu, M.; Papavassiliou, D. V. Scalable, eco-friendly and ultrafast solar steam generators based on one-step melamine-derived carbon sponges toward water purification. *Nano Energy* **2019**, *58*, 322−330.
(30) Shi, Y.; Zhang, C.; Wang, Y.; Cui, Y.; Wang, Q.; Liu, G.; Gao, S.; Yuan, Y. Plasmonic silver nanoparticles embedded in flexible three-dimensional carbonized melamine foam with enhanced solar-driven water evaporation. *Desalination* **2021**, *507*, No. 115038.
(31) Lee, A. Y.; Yang, K.; Anh, N. D.; Park, C.; Lee, S. M.; Lee, T. G.; Jeong, M. S. Raman study of D* band in graphene oxide and its correlation with reduction. *Appl. Surf. Sci.* **2021**, *536*, No. 147990.
(32) Maslova, O. A.; Ammar, M. R.; Fantini, C.; Barannikova, S. A.; Pimenta, M. A. Resonant Raman scattering of anthracene-based carbons in the secondary carbonization stage. *J. Raman Spectrosc.* **2021**, *52*, 670−677.
(33) Jiang, X. D.; Xu, W. R.; Ilyas, N.; Li, M. C.; Guo, R. K.; Khan, R.; Li, W.; Wang, J. M. High-Performance coupled plasmon waveguide resonance optical sensor based on SiO_2: Ag film. *Res. Phys.* **2021**, *26*, 8.
(34) Jiang, Y.; Smolentsev, S.; Jun, J.; Pint, B.; Kessel, C. Prediction of PbLi fluid flow and temperature field in a thermal convection loop for qualification of fusion materials. *Int. J. Heat Mass Transfer* **2021**, *172*, 14.
(35) Xie, B. Q.; Lovell, E.; Tan, T. H.; Jantarang, S.; Yu, M. Y.; Scott, J.; Amal, R. Emerging material engineering strategies for amplifying photothermal heterogeneous CO2 catalysis. *J. Energy Chem.* **2021**, *59*, 108−125.
(36) Xue, J. L.; Xu, L. L.; Wang, T. T.; Fan, Y. X.; Tao, Z. Y. Terahertz Thermal Sensing by Using a Defect-Containing Periodically Corrugated Gold Waveguide. *Appl. Sci.* **2020**, *10*, 11.
(37) Zhang, W. B.; Shen, Z. Z.; Ren, J.; Gan, L.; Wang, F.; Yu, B. H.; Li, C. L. Modeling and comparative analysis of a flow and heat coupling model of the riparian zone based on thermal conductivity empirical models. *J. Hydrol.* **2020**, *582*, 16.
(38) Fuzil, N. S.; Othman, N. H.; Alias, N. H.; Marpani, F.; Othman, M. H. D.; Ismail, A. F.; Lau, W. J.; Li, K.; Kusworo, T. D.; Ichinose, I.;

https://doi.org/10.1021/acsami.2c03124
ACS Appl. Mater. Interfaces 2022, 14, 23400−23407

Shirazi, M. M. A. A review on photothermal material and its usage in the development of photothermal membrane for sustainable clean water production. *Desalination* **2021**, *517*, 28.
(39) Kim, D. M.; Park, J. S.; Jung, S. W.; Yeom, J.; Yoo, S. M. Biosensing Applications Using Nanostructure-Based Localized Surface Plasmon Resonance Sensors. *Sensors* **2021**, *21*, 3191.
(40) Tontarawongsa, S.; Visitsattapongse, S.; Pechprasarn, S. Performance Analysis of Non-Interferometry Based Surface Plasmon Resonance Microscopes. *Sensors* **2021**, *21*, 17.
(41) Nurrohman, D. T.; Chiu, N. F. A Review of Graphene-Based Surface Plasmon Resonance and Surface-Enhanced Raman Scattering Biosensors: Current Status and Future Prospects. *Nanomaterials* **2021**, *11*, 29.
(42) Wang, N. N.; Feng, Y. G.; Zheng, Y. B.; Zhou, F.; Wang, D. A. Triboelectrification of interface controlled by photothermal materials based on electron transfer. *Nano Energy* **2021**, *89*, 11.

https://doi.org/10.1021/acsami.2c03124
ACS Appl. Mater. Interfaces 2022, 14, 23400−23407